ChemPubSoc Europe

DOI: 10.1002/chem.201901400

CHEMISTRY A European Journal Full Paper

Electrochemistry |*Hot Paper*|

Transition-Metal Oxides/Carbides@Carbon Nanotube Composites as Multifunctional Electrocatalysts for Challenging Oxidations and Reductions

Xiaolin Xing,[a] Rongji Liu,*[a, b] Kecheng Cao,[c] Ute Kaiser,[c] and Carsten Streb*[a, d]

Abstract: The rapid development of renewable-energy technologies such as water splitting, rechargeable metal–air batteries, and fuel cells requires highly efficient electrocatalysts capable of the oxygen-reduction reaction (ORR) and the oxygen-evolution reaction (OER). Herein, we report a facile sonication-driven synthesis to deposit the molecular manganese vanadium oxide precursor $[Mn_4V_4O_{17}(OAc)_3]^{3-}$ on multiwalled carbon nanotubes (MWCNTs). Thermal conversion of this composite at 900 °C gives nanostructured manganese vanadium oxides/carbides, which are stably linked to the MWCNTs. The resulting composites show excellent electrochemical reactivity for ORR and OER, and significant reactivity enhancements compared with the precursors and a Pt/C reference are reported. Notably, even under harsh acidic conditions, long-term OER activity at low overpotential is reported. In addition, we report exceptional activity of the composites for the industrially important Cl_2 evolution from an aqueous HCl electrolyte. The new composite material shows how molecular deposition routes leading to highly active and stable multifunctional electrocatalysts can be developed. The facile design could in principle be extended to multiple catalyst classes by tuning of the molecular metal oxide precursor employed.

1. Introduction

Bifunctional catalysts for the oxygen-evolution reaction (OER) and the oxygen-reduction reaction (ORR) play an important role in efficient energy conversion and storage as they are used in fuel cells, metal–air batteries, and water electrolyzers. Developing new, efficient bifunctional OER/ORR electrocatalysts based on earth-abundant materials is therefore crucial for the future deployment of these technologies.[1–7] To date, most well-established OER electrocatalysts such as ruthenium or iridium oxides show low ORR activity, whereas highly efficient ORR electrocatalysts, for example, Pt, show only moderate OER activity. Furthermore, the high cost of noble-metal catalysts makes their large-scale use prohibitively expensive.[8–11] Recently, transition-metal oxides and carbides have been put forward as alternative ORR and OER electrocatalysts that can show catalytic performance similar to noble metals.[12–18] Currently, these materials are still hampered by their low electrical conductivity and their fast degradation due to irreversible redox processes on the surface of the material. One approach to overcome these issues is the design of nanostructured composites in which the reactive transition-metal oxides or carbides are electrically "wired" to conductive carbon substrates; this leads to high-performance electrocatalysts, for example, for ORR and/or OER.[19–23] Although top-down syntheses of transition-metal oxide/carbide–carbon composites have been explored in detail, the bottom-up fabrication of such composites starting from molecular metal oxide precursors has only recently become a focus in the design of energy materials.[24–26]

In this work, we used manganese vanadium oxide cluster anions as molecular precursors for metal oxides and carbides. The approach is based on the established high electrocatalytic reactivity of this compound class so that we expected high performance for ORR and OER when deposited on high-surface-area carbon nanotubes. Although molecular polyoxometalates (POMs) are well known for their multielectron transfer reactivity (e.g., for the OER, ORR, and hydrogen-evolution reactions),[27–30] their stable linkage to conductive substrates is still a challenge owing to their solubility in many common electrolytes, particularly in water.[25] One viable materials design strategy is the controlled deposition and conversion of POMs into nanostructured solid-state metal oxides or carbides. The concept has recently been explored by us and others for manga-

[a] X. Xing, Dr. R. Liu, Prof. C. Streb
Institute of Inorganic Chemistry I
Ulm University, Ulm, 89081 (Germany)
E-mail: rongji.liu@uni-ulm.de
carsten.streb@uni-ulm.de

[b] Dr. R. Liu
Institute of Process Engineering
Key Laboratory of Green Process and Engineering
Chinese Academy of Sciences, Beijing, 100190 (China)

[c] K. Cao, Prof. U. Kaiser
Central Facility of Electron Microscopy for Materials Science
Ulm University, Ulm, 89081 (Germany)

[d] Prof. C. Streb
Helmholtz-Institute Ulm for Electrochemical Energy Conversion
Ulm, 89081 (Germany)

Supporting information and the ORCID identification number(s) for the author(s) of this article can be found under:
https://doi.org/10.1002/chem.201901400.

nese vanadium POMs owing to their high redox reactivity coupled with the ability to store and transfer multiple electrons, which leads to new nanostructured Mn-V-oxide OER catalysts[31,32] as well as Mn-V-oxide/graphene quantum dot composites for high-performance lithium-ion batteries.[33] Therefore, the deposition of Mn-V-oxides and -carbides based on the corresponding Mn-V-based POMs on nanostructured carbon could be an ideal approach for highly active electrocatalyst design.

Nanostructured carbon and in particular carbon nanotubes (CNTs) are ideally suited for the anchoring of POM-based catalysts as they offer a high specific surface area, they can be oxidatively surface-functionalized (leading to surface –OH and –COOH groups suitable for metal oxide anchoring), are electrically conductive, and thermally and chemically highly stable. Significant research has gone into developing CNT-based composites for electrocatalytic applications.[34–37] However, the electronically and chemically stable linkage between charge-transport sites (i.e., CNTs) and redox-active components (e.g., metal oxides and carbides) is still a bottleneck, so many composites lack long-term stability and show poor interfacial conductivity. Therefore, new design concepts are still required that lead to enhanced linkage between the metal oxides/carbides and carbon components.

Herein, we report a facile deposition route, which allows the intimate linkage of metal oxides/carbides and CNT substrates while maintaining the chemical reactivity of both components. The composites combined high OER and ORR activity with low overpotentials and high current densities. Notably, for the OER, the composites showed high electrocatalytic activity both in alkaline and acidic electrolytes. It is noteworthy that the as-prepared composites exhibited high activity and stability for aqueous HCl electrolysis, which indicates a promising potential for industry application. Therefore, the results could open new design paths to multifunctional composites based on earth-abundant materials for both oxidative and reductive electrocatalysis.

2. Results and Discussion

2.1. Synthesis

The synthetic approach for the composite design is shown in Scheme 1. Multiwalled carbon nanotubes (MWCNTs) were pretreated with concentrated HNO_3 (65%) to introduce oxidized surface carbon groups (e.g., –COH, –COOH) suitable for metal oxide anchoring. For the manganese vanadate precursor, we employed the organo-soluble $[Mn_4V_4O_{17}(OAc)_3]^{3-}$ (={Mn_4V_4}) prototype,[38] the conversion of which to manganese vanadium oxide nanoparticles has already been established.[39] For the deposition of the precursor on multiwalled CNTs, we used a recently established mild sonication route.[33,40] Stable anchoring of the metal oxides and carbides on the MWCNTs was then achieved by calcination of the composite at 600, 750, and 900 °C. The samples obtained were designated as **1-600**, **1-750**, and **1-900**, respectively.

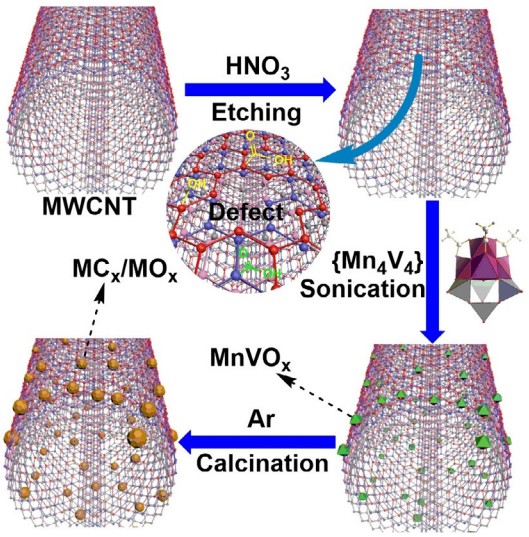

Scheme 1. Schematic illustration of the synthesized composites (MC_x/MO_x = Mn_7C_3/V_8C_7/MnO).

2.2. Characterization

Powder X-ray diffraction (pXRD) was used to follow the structure changes within the composites as a function of calcination temperature. As shown in Figure 1, the non-calcined sample gave only one diffraction signal at $2\theta \approx 26°$ that corresponded to the (002) plane of the CNTs. At a calcination temperature of 600 °C, the formation of crystalline MnV_2O_4 (PDF#39-0038) was observed (Figure S1a in the Supporting Information). At a calcination temperature of 750 °C, a mixture of MnV_2O_4 and MnO (PDF#07-0230) was observed (Figure S1b).

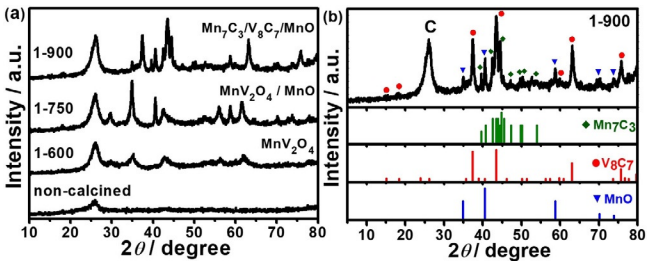

Figure 1. Powder X-ray diffraction of a) composites prepared at different temperatures and b) **1-900** with specified peaks.

Only at a calcination temperature of 900 °C was the formation of crystalline metal carbide species observed, and pXRD analyses allowed the identification of a mixture of Mn_7C_3 (PDF#36-1269), V_8C_7 (PDF#35-0786), and MnO (PDF#07-0230), respectively (Figure 1b).

Aberration-corrected high-resolution transmission electron microscopy (AC-HRTEM) was performed to examine the structure of the composites. Compound **1-900** (Figure 2a) showed the presence of intact MWCNTs with particles deposited on the surface. Subsequent HRTEM images of the particles (Figure 2b–d) gave lattice spacings in line with MnO, Mn_7C_3, and V_8C_7, which is in agreement with the results of the pXRD analysis.

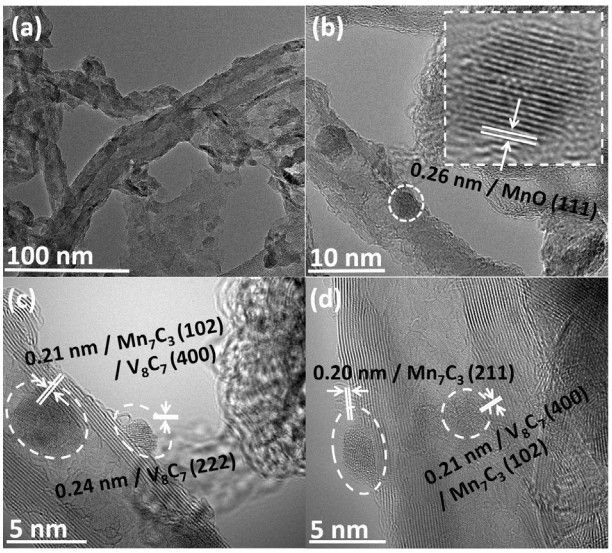

Figure 2. High-resolution transmission electron microscopy (HRTEM) images of **1-900** showing the metal oxide/carbide nanoparticles attached to the MWCNT surface.

The particles were in the low nanometer range (diameter ≈4–5 nm) and were stably attached to the MWCNT surface, which allows them to be accessible for solid–liquid electrochemical reactions.

X-ray photoelectron spectroscopy (XPS) was performed to explore the composition and chemical properties of **1-900**. The survey spectrum (Figure 3a) identified the presence of Mn, V, C, and O. The atomic ratio between Mn and V was approximately 1, which is consistent with the inductively coupled plasma mass spectrometry (ICP-MS) results (Mn: 10.9 wt%; V: 10.6 wt%). Figure 3b shows the deconvoluted XPS spectrum for the Mn 2p region, which indicates the expected presence of Mn–C (carbide) and Mn–O (oxide) bonds.[41,42] The Mn 3s peak (Figure 3c) shows two multiplet split components, which are caused by 3s–3d electronic coupling (peak separation: 5.9 eV); this indicates the presence of Mn^{II} in MnO (expected peak separation: 6.0 eV).[43] The deconvoluted V 2p spectrum (Figure 3d) indicates the presence of V–C (carbide) bonds, which is in line with the formation of V_8C_7,[44] as well as peaks assigned to V $2p_{3/2}$ and V $2p_{1/2}$. Analysis of the deconvoluted C 1s spectrum (Figure 3e) indicates the presence of C–C, C–V, C–O–C, and O–C=O, respectively. For O 1s (Figure 3f), the deconvoluted XPS spectrum can be assigned to the oxygen–metal (Mn, V) bonds and oxygen–carbon bonds.[42]

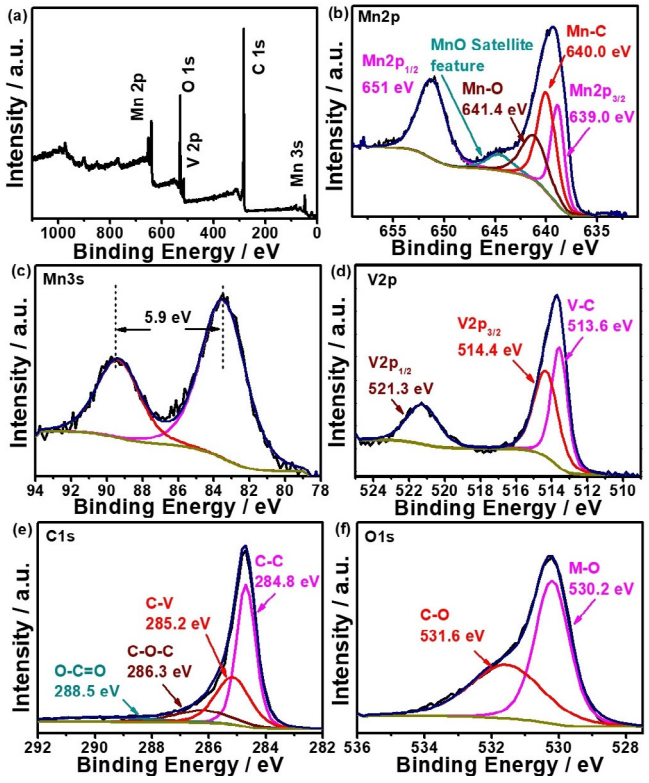

Figure 3. a) Overview XPS spectra for **1-900** and b)–f) deconvoluted XPS spectra of Mn, V, C, and O for **1-900**.

2.3. ORR activity

The electrocatalytic ORR activity of the composites was firstly studied by using a rotating disk electrode (RDE) technique with linear sweep voltammetry (LSV) in O_2-saturated 0.1 M aqueous KOH. As shown in Figure 4a, **1-900** features a positive onset reduction potential of 0.94 V (relative to the reversible hydrogen electrode (RHE)) independent of the rotation speed, together with high limiting current densities (J_d). Further analysis of the electrochemical data using Koutecky–Levich (K–L) plots at potentials between 0.60 and 0.80 V (vs. RHE) indicates first-order reaction kinetics with respect to the dissolved oxygen concentration (Figure 4b).

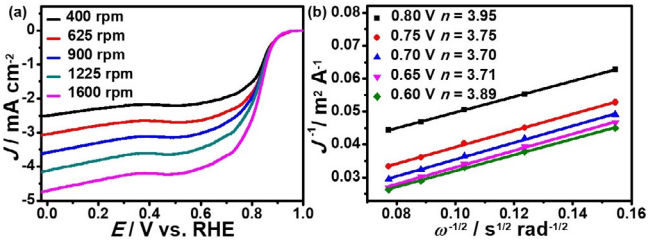

Figure 4. a) LSV analysis of **1-900** in O_2-saturated 0.1 M aqueous KOH solution at different rotation rates; b) Koutecky–Levich plots for **1-900** (plot of J^{-1} versus $\omega^{-1/2}$) at different electrode potentials.

Based on the K–L plot slopes, the electron-transfer number (n) was calculated to be approximately 3.8 (calculated between 0.60 and 0.80 V vs. RHE),[45] which suggests that the ORR catalyzed by **1-900** proceeds by means of a four-electron pathway.[46] Next, we explored how different calcination temperatures affect the catalytic ORR performance. To this end, we evaluated the composites calcined at 600 °C (**1-600**) and 750 °C (**1-750**). Both composites contain MnV_2O_4 as the main crystalline phase. In addition, **1-750** also features MnO as the second crystalline metal oxide phase (Figure S1 in the Supporting Information). Both composites do not contain any metal carbide species (for detailed characterization, see the Supporting Infor-

mation). For both reference composites, we performed electrochemical ORR measurements under identical experimental conditions as those described above. For both **1-600** and **1-750**, we observed similar reactivity with comparable onset potentials (0.90 and 0.88 V vs. RHE, respectively), electron-transfer number ($n \approx 3.9$), and virtually identical current densities (see Figures S2 and S3). In contrast, the pure CNT reference showed lower ORR activity with a less positive onset potential (E_{onset}, 0.8 V vs. RHE), lower electron-transfer number ($n \approx 3.2$, which indicates the contribution of a two-step two-electron pathway), and lower J_d (Figure S4).

Next, we used rotating ring-disk electrode (RRDE) electrochemical analyses to gain further insight into the ORR mechanism. As reported earlier, two different pathways are described for O_2 reduction: in the two-electron transfer process, O_2 is initially reduced by two electrons with the peroxide species (HO_2^-) as an intermediate, followed by a further two-electron reduction to hydroxide (OH^-). In contrast, the four-electron process proceeds by direct reduction of O_2 to OH^- in a four-electron mechanism.[45] Therefore, determination of HO_2^- formation by RRDE measurements is a reliable means to identify the ORR catalytic pathway. Figure 5a shows the disk and ring current densities recorded by RRDE-LSV at 1600 rpm in 0.1 M aqueous KOH electrolyte for the as-prepared **1-900** composites, and references of pure CNTs and commercial Pt/C (20 wt%). Note that at identical potentials, the **1-900** sample showed comparable ORR activities to commercial Pt/C (20 wt%) based on E_{onset}, half-wave potential ($E_{1/2}$), and J_d values (for details, see Table 1). In contrast, the pure CNTs featured significantly lower disk currents and less positive E_{onset} compared with the composite. The HO_2^- yields and electron-transfer numbers from the RRDE data are shown in Figure 5b. Data analysis shows that composite **1-900** produced a similar percentage of HO_2^- with similar average electron-transfer numbers ($n \approx 3.9$) as Pt/C (20 wt%). This is in line with the RDE data reported above. Furthermore, the Tafel slopes for the composites were also significantly lower than those of the non-modified CNTs and even lower than Pt/C (20 wt%) (**1-900**: 58 mV dec^{-1}; pure CNTs: 180 mV dec^{-1}; Pt/C: 88 mV dec^{-1}, see Figure S5). The lower Tafel slope observed for the composite suggests favorable ORR catalytic kinetics, which emphasizes the synergism between the metal oxide/carbide reaction sites and the CNT supports.

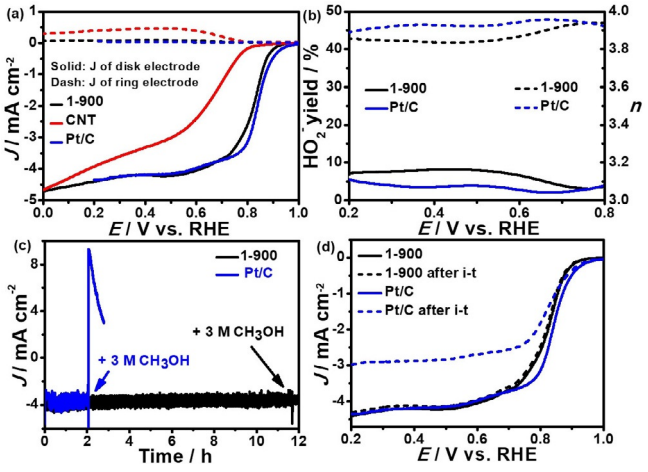

Figure 5. a) RRDE linear-sweep voltammogram of **1-900**, pure CNT reference, and commercial Pt/C (20 wt%) reference in O_2-saturated 0.1 M aqueous KOH at 1600 rpm. The disk potential was scanned at 10 mV s^{-1} and the ring potential was kept constant at 1.45 V (vs. RHE). b) Percentage of peroxide species (HO_2^-) formed with respect to the total oxygen-reduction products and the electron-transfer number (n) based on the RRDE data in (a). The solid line indicates the percentage of peroxide species and the dashed line indicates the electron-transfer number n. c) Methanol tolerance evaluation for **1-900** and commercial Pt/C (20 wt%) tested by chronoamperometry at 0.65 V (vs. RHE). d) LSV stability test before and after chronoamperometry for 12 h. Catalyst loading was 0.3 mg cm^{-2} for all samples.

Table 1. Comparison of ORR and OER performance in 0.1 M aqueous KOH solution, ECSA, and R_{ct} of the composites studied.[a]

Cat.	$E_{onset\ (ORR)}$ [V][b]	$E_{1/2\ (ORR)}$ [V][b]	E_{OER} at $J = 10$ mA cm^{-2} [V][b]	$\Delta E_{OER-ORR}$ [V][b]	ECSA [cm^2]	R_{ct} [ohm]
1-600	0.90	0.78	1.68	0.90	478	23.4 ± 2.0
1-750	0.88	0.78	1.75	0.97	278	40.5 ± 3.0
1-900	0.94	0.82	1.60	0.78	5150	3.6 ± 0.4
Pt/C	0.96	0.84	> 2.00	> 1.2	–	–

[a] $E_{RHE} = E_{Ag/AgCl} + E^{\circ}_{Ag/AgCl} + 0.059\,pH$ in which E_{RHE} is the converted potential versus a RHE; $E_{Ag/AgCl}$ is the experimental potentials measured against the Ag/AgCl reference electrode, respectively; $E^{\circ}_{Ag/AgCl}$ is the standard potential of Ag/AgCl at 25 °C. [b] All values are with reference to a RHE.

We further explored the chemical stability and methanol tolerance (a well-known ORR catalyst poison, particularly for noble-metal catalysts)[47–49] of the composites under electrocatalytic ORR conditions by chronoamperometric studies in 0.1 M aqueous KOH solution. As shown in Figure 5c, **1-900** was highly resistant to the presence of MeOH (3 M) and showed no change in current upon MeOH addition. In contrast, the commercial Pt/C (20 wt%) catalyst showed a large current increase upon MeOH addition, which indicates the occurrence of MeOH-based side reactions on Pt/C (20 wt%). The chemical stability of the composites can be further evaluated by comparing the response by LSV and cyclic voltammetry (CV) before and after chronoamperometry (*i–t* test, electrolysis time: 12 h). Composite **1-900** showed virtually no changes in both E_{onset} and current density (Figure 5d), as well as the CV voltammograms before and after the *i–t* test (see Figure S6), whereas the Pt/C (20 wt%) reference showed a significant negative shift of the $E_{1/2}$ (≈ −60 mV) and decreased current density (≈ −30%), thereby highlighting the excellent durability of the new composites. In addition, the morphology of catalyst **1-900** after the *i–t* test was also studied by HRTEM (see Figure S7), and the stably anchored nanoparticles on the surface of the CNTs suggested its stable structure and a high chemical resistance of the catalyst.

2.4. OER activity

Based on the well-known oxidative reactivity of manganese vanadium oxides,[39] we explored the OER activity of the composite materials under technologically relevant alkaline (0.1 M

aqueous KOH) and acidic (0.5 M aqueous H_2SO_4) conditions. First, we performed RDE electrochemical analyses in 0.1 M aqueous KOH. As shown in Figure 6, **1-900** features promising OER activity and shows more negative onset potentials and higher current densities than commercial Pt/C (20 wt%). For

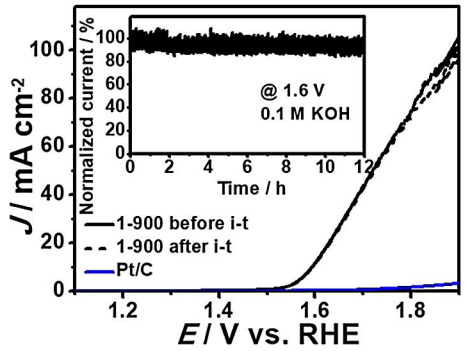

Figure 6. Linear sweep voltammograms (LSV) of **1-900** and commercial Pt/C (20 wt%) in 0.1 M aqueous KOH. Inset: Chronoamperometric stability test for **1-900** at 1.6 V (vs. RHE) for 12 h. LSV conditions: rotation rate: 1600 rpm; O_2-saturated aqueous solution; scan rate: 10 mV s^{-1}; catalyst loading: 0.3 mg cm^{-2}.

comparison, we determined the oxygen-evolution potential at a current density of 10 mA cm^{-2}, which is used as a standardized reference in OER catalysis.[50] Composite **1-900** (Figure 6) showed the best activity with a potential of 1.60 V (vs. RHE) at $J = 10$ mA cm^{-2}, whereas **1-600** and **1-750** (Figure S8) showed much lower activity, which suggests that the presence of metal carbides might contribute to the high reactivity.[12,13,51] The commercial Pt/C (20 wt%) did not reach a current density of 10 mA cm^{-2}, even at a potential of approximately 2.0 V (vs. RHE). Analysis of the Tafel slopes for the composites gave values of 127 (**1-600**), 127 (**1-750**), 70 (**1-900**), and 296 mV dec^{-1} (Pt/C) (Figure S9), which highlights the superior OER-catalytic kinetics of **1-900**. The long-term OER stability of **1-900** was demonstrated by chronoamperometry at a potential of 1.6 V (vs. RHE) for 12 h, during which virtually no change in the current was observed (inset in Figure 6). Further LSV (Figure 6) and CV (Figure S10) analyses before and after chronoamperometry also showed only marginal changes, which further highlights the high stability of **1-900** under oxidative conditions.

To gain further insights into the stability window of the composites, we examined the OER activity of **1-900** in acidic electrolyte (0.5 M aqueous H_2SO_4) using RDE-LSV studies. As shown in Figure S11 in the Supporting Information, **1-900** showed high OER activity and featured an oxygen-evolution potential (at $J = 10$ mA cm^{-2}) of 1.64 V. Commercial Pt/C (20 wt%) as reference did not reach the desired current densities under the given experimental conditions. In contrast, **1-600** and **1-750** also showed lower activity in acidic medium (see Figure S12). Kinetic analyses gave Tafel slopes of 321, 343, 300, and 451 mV dec^{-1} for **1-600**, **1-750**, **1-900**, and Pt/C (20 wt%) respectively (see Figure S13). We also analyzed the electrochemical stability by chronoamperometry at a potential of 1.64 V (vs. RHE) for 12 h (inset in Figure S11). From the comparison of LSV (Figure S11) and CV (Figure S14) analyses before and after chronoamperometry, only slight potential shifts were observed, which highlights the long-term stability and high chemical resistance of the materials under acidic conditions.

Finally, we analyzed the potential difference between OER and ORR ($\Delta E_{OER-ORR}$) in 0.1 M aqueous KOH for the composites reported: the smallest potential difference was observed for **1-900** ($\Delta E_{OER-ORR} = 0.78$ V), which is significantly lower than various noble-metal-based references such as 20 wt% Pt/C (1.16 V), 20 wt% Ir/C (0.92 V),[52] 20 wt% Ru/C (1.01 V),[53] IrO_2 (1.11 V),[54] RuO_2 (1.30 V),[19] as well as various metal-free carbon-nanotube-based materials and transition-metal oxide modified carbon materials.[55,56] For a detailed comparison, see Table 1 and Table S1. In summary, the as-prepared composites acted as a highly active and highly stable bifunctional electrocatalyst for both OER and ORR.

2.5. Chlorine evolution activity

Based on the high stability and reactivity of **1-900** under harsh oxidative conditions, we examined the electrocatalytic Cl_2 evolution by the composite using RDE analyses in 1 M aqueous HCl electrolyte. As shown in Figure 7, **1-900** showed a Cl_2 evolution E_{onset} of 1.42 V (vs. RHE) at $J = 10$ mA cm^{-2} (Tafel slope = 116 mV dec^{-1}, Figure S15). In addition, high current densities greater than 400 mA cm^{-2} (at $E = 1.8$ V vs. RHE) were observed. To provide evidence for chloride oxidation, we performed comparative LSV studies in Cl^- free electrolyte (1 M aqueous H_2SO_4). Here, virtually no electrocatalytic activity was observed. However, upon addition of NaCl (1 M) to the electrolyte, the electrocatalytic reactivity was recovered (see Figure 7). The stability of **1-900** for Cl_2 evolution was investigated by CV cycling between 1.0 and 1.6 V (vs. RHE).

As shown in Figure 7, the LSV before and after CV cycling (1000 cycles) showed only minor changes for E_{onset} and current density, thereby verifying the high chemical stability of the composite under oxidative conditions.

To gain further mechanistic insights into the superior electrocatalytic performance of **1-900**, electrochemical impedance spectroscopy (EIS) was performed (Figure S16), and a simplified

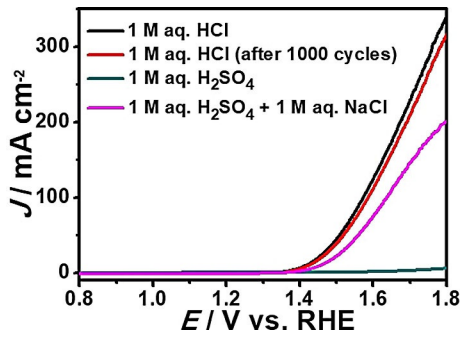

Figure 7. LSV of **1-900** in 1 M aqueous HCl and 1 M aqueous H_2SO_4 electrolyte. Conditions: Ar-saturated aqueous solution; scan rate: 10 mV s^{-1}; counter electrode: graphite rod; reference electrode: saturated calomel electrode; catalyst loading: 0.3 mg cm^{-2}; rotation rate: 1600 rpm.

equivalent circuit (inset in Figure S16) was used to explain the measured results. Composite **1-900** showed the lowest charge-transfer resistance (R_{ct}, Table 1) of all materials analyzed here, which indicates an efficient charge transfer in **1-900**. This is also consistent with the lowest Tafel slopes observed for this composite in ORR/OER catalysis. Furthermore, we analyzed the electrochemical double-layer capacitance (C_{dl}) to calculate the electrochemical surface area (ECSA, Table 1, see the detailed calculation in the Supporting Information) based on the CV recorded in the non-Faradic region at different scan rates (Figure S17). Here, **1-900** exhibited significantly higher ECSA than **1-600** and **1-750**, which is most likely a significant contributor to the high reactivity observed.

3. Conclusion

In summary, a highly efficient, noble-metal-free multifunctional electrocatalyst composite is reported that is capable of performing ORR, OER, and hydrochloric acid electrolysis. Facile synthetic access using a one-pot assembly route is reported in which nanoscale manganese/vanadium carbide/oxide particles are deposited on surface-functionalized multiwalled carbon nanotubes. Electrocatalytic studies demonstrate the long-term stability of the composites and emphasize the robust anchoring of the metal carbides/oxides on the CNT surface. For both ORR and OER, we report low overpotentials, high current densities, and long-term stability. Of particular importance is the good reactivity of the composites under acidic OER conditions, which is still challenging for many state-of-the-art materials. It is worth noting that the **1-900** composites showed excellent activity and high stability for chlorine evolution in aqueous HCl electrolyte, which could be a promising candidate for further HCl electrolysis application. The same protocol could be used for the designing of novel mixed-metal carbides/oxides as (electro-)catalysts for challenging multielectron-transfer reactions.

4. Experimental Section

Synthesis of the composite materials

In a typical synthesis, carbon nanotubes (2.0 g) were suspended in concentrated nitric acid (45 g, ≈65 wt%) and heated at reflux under magnetic stirring for 48 h at 140 °C (oil-bath temperature). The resulting dispersion was carefully diluted with water (ca. 20 mL) and filtered. The resulting solid was washed until the filtrate was pH neutral and the sample was dried at 100 °C overnight. Deposition of the manganese vanadium crystal particles was achieved by sonicating the CNTs (500 mg) in acetonitrile (100 mL) for 5 min and subsequent addition of $[Mn_4V_4O_{17}(OAc)_3]^{3-}$ (250 mg, 0.15 mmol dissolved in 100 mL acetonitrile). The mixture was sonicated for 1 h using a pulsed high-frequency sonicator (180 W). The black precipitate formed was collected by centrifugation, washed thoroughly with ethanol, and dried at 40 °C for 12 h. Then the dried black product was heated in a tube furnace (heating rate 10 °C min^{-1}, Ar flow), kept at 900 °C for 4 h, and cooled to room temperature under an Ar atmosphere; the obtained composite was named **1-900**. The composites obtained by a similar heating step but with calcination performed at 600 and 750 °C were named **1-600** and **1-750**, respectively.

Characterization

High-resolution transmission electron microscopy (HRTEM) measurements were performed with an image-side-aberration-corrected FEI TITAN 80-300 under an accelerating voltage of 80 kV. Powder X-ray diffraction (pXRD) studies were performed on a BRUKER D8 Advance XRD unit using $Cu_{K\alpha}$ ($\lambda = 1.54$ Å) radiation. X-ray photoelectron spectroscopy (XPS) was performed on ESCALAB250 Thermo Electron Corporation equipment with an $Al_{K\alpha}$ X-ray source (1486.6 eV). The X-ray source was run at a reduced power of 150 W, and the pressure in the analysis chamber was maintained at 10–11 Pa or lower. All chemicals were purchased from Sigma Aldrich, ABCR, or ACROS and were of reagent grade. The chemicals were used without further purification unless stated otherwise. $(n\mathrm{Bu_4N})_4[Mn_4V_4]$ was prepared according to the literature.[37]

Electrochemical studies

All electrochemical measurements were performed on an electrochemical workstation (CHI 730 E, CH Instruments, Inc. USA) at room temperature using a standard three-electrode electrochemical cell. For measurements in alkaline electrolyte, a Pt wire and an Ag/AgCl electrode in 3 M aqueous KCl were used as the counter and reference electrodes, respectively. For measurements in acidic electrolyte, a graphite rod and a saturated calomel electrode (SCE) in saturated aqueous KCl were used as the counter and reference electrodes, respectively. All potentials in this study are given versus the reversible hydrogen electrode (RHE): $E(\mathrm{RHE}) = E(\mathrm{Ag/AgCl}) + 0.210 + 0.059\,\mathrm{pH}$ in which 0.210 V is the standard potential for the Ag/AgCl electrode at 25 °C; $E(\mathrm{RHE}) = E(\mathrm{SCE}) + 0.241 + 0.059\,\mathrm{pH}$, in which 0.241 V is the standard potential for the SCE electrode at 25 °C. A glassy carbon rotating disk electrode (RDE) with 4.0 mm diameter and a rotating Pt ring glassy carbon disk electrode (RRDE, disk diameter 4.0 mm; Pt ring: inner diameter 6.0 mm; outer diameter 8.0 mm) was used as the working electrode to evaluate the electrochemical catalytic performance.

For all electrochemical measurements, the modified electrodes were used as working electrodes and were prepared by the following method: the as-prepared catalyst (4 mg), Nafion solution (20 μL, 5 wt% in water and 1-propanol, Nafion D-520, Germany), and ethanol (2 mL) were mixed for at least 1 h of sonication to form a homogeneous ink. The catalyst ink (18.8 μL) was pipetted onto the surface of the glassy carbon working electrode and air-dried. Unless stated otherwise, the catalyst loading was 0.3 mg cm^{-2}. For comparison, a commercial Pt/C (20 wt% Pt on Vulcan carbon black from Premetek Co.) was deposited on the working electrode by using the same procedure and was tested for ORR and OER under identical conditions.

For the ORR measurements, the modified RDE was used as the working electrode and the experiment was performed in an O_2-saturated solution using LSV at a scan rate of 10 mV s^{-1} with a rotating rate from 400 to 1600 rpm.

To study the activity and selectivity of the catalyst for oxygen reduction, the modified RRDE was used as the working electrode and the LSV was recorded at a scan rate of 10 mV s^{-1} at 1600 rpm, and the ring potential was kept at 1.45 V (vs. RHE).

Acknowledgements

Ulm University, the Deutsche Forschungsgemeinschaft (STR1164/4, STR1164/12, TRR234 "CataLight", projects A4 and C4), Helmholtz-Institute Ulm (HIU), the National Natural Science Foundation of China (no. 91545125), and Chinese Academy of Sciences President's International Fellowship Initiative (2018VMA0041) are acknowledged for financial support. X.X and K.C. acknowledge the China Scholarship Council (CSC) for financial support. U.K. acknowledges the support of the Graphene Flagship and the DFG and the Ministry of Science, Research and the Arts (MWK) of Baden-Wuerttemberg within the framework of the SALVE (sub-Angstrom low-voltage electron microscopy) project. R.L. acknowledges the Alexander-von-Humboldt-Foundation for a postdoctoral fellowship.

Conflict of interest

The authors declare no conflict of interest.

Keywords: electrocatalysis · electrochemistry · organic–inorganic hybrid composites · oxygen evolution · polyoxometalates

[1] S. Ghosh, P. Kar, N. Bhandary, S. Basu, S. Sardar, T. Maiyalagan, D. Majumdar, S. K. Bhattacharya, A. Bhaumik, P. Lemmens, S. K. Pal, *Catal. Sci. Technol.* **2016**, *6*, 1417.
[2] Y. Gorlin, B. Lassalle-Kaiser, J. D. Benck, S. Gul, S. M. Webb, V. K. Yachandra, J. Yano, T. F. Jaramillo, *J. Am. Chem. Soc.* **2013**, *135*, 8525.
[3] M. Prabu, P. Ramakrishnan, P. Ganesan, A. Manthiram, S. Shanmugam, *Nano Energy* **2015**, *15*, 92.
[4] P. Ganesan, M. Prabu, J. Sanetuntikul, S. Shanmugam, *ACS Catal.* **2015**, *5*, 3625.
[5] G. Chen, S. R. Bare, T. E. Mallouk, *J. Electrochem. Soc.* **2002**, *149*, A1092.
[6] Z. Chen, Z. Chen, A. Yu, R. Ahmed, H. Wang, H. Li, *Electrochim. Acta* **2012**, *69*, 295.
[7] Z. Yan, H. Qi, X. Bai, K. Huang, Y. R. Chen, Q. Wang, *Electrochim. Acta* **2018**, *283*, 548.
[8] G. Wu, K. L. More, C. M. Johnston, P. Zelenay, *Science* **2011**, *332*, 443.
[9] Y. Hou, Z. Wen, S. Cui, S. Ci, S. Mao, J. Chen, *Adv. Funct. Mater.* **2015**, *25*, 872.
[10] Z. Xiang, Y. Xue, D. Cao, L. Huang, J. F. Chen, L. Dai, *Angew. Chem. Int. Ed.* **2014**, *53*, 2433; *Angew. Chem.* **2014**, *126*, 2465.
[11] Y. Cheng, C. Liu, H.-M. Cheng, S. P. Jiang, *ACS Appl. Mater. Interfaces* **2014**, *6*, 10089.
[12] D. J. Ham, J. S. Lee, *Energies* **2009**, *2*, 873.
[13] H. H. Hwu, J. G. Chen, *Chem. Rev.* **2005**, *105*, 185 – 212.
[14] T. G. Kelly, J. G. Chen, *Chem. Soc. Rev.* **2012**, *41*, 8021.
[15] R. Lang, W. Xi, J. C. Liu, Y. T. Cui, T. Li, A. F. Lee, F. Chen, Y. Chen, L. Li, L. Li, J. Lin, S. Miao, X. Liu, A. Q. Wang, X. Wang, J. Luo, B. Qiao, J. Li, T. Zhang, *Nat. Commun.* **2019**, *10*, 234.
[16] X. Bai, Q. Wang, G. Xu, Y. Ning, K. Huang, F. He, Z. J. Wu, J. Zhang, *Chem. Eur. J.* **2017**, *23*, 16862.
[17] Z. Shao, J. Sun, N. Guo, F. He, K. Huang, F. Tian, Q. Wang, *J. Power Sources* **2019**, *422*, 33.
[18] Z. Y. Shao, H. Qi, X. Wang, J. Sun, N. K. Guo, K. Huang, Q. Wang, *Electrochim. Acta* **2019**, *296*, 259.
[19] T. Li, Y. Lu, S. Zhao, Z. D. Gao, Y. Y. Song, *J. Mater. Chem. A* **2018**, *6*, 3730.
[20] X. Zhao, F. Li, R. Wang, J. M. Seo, H. J. Choi, S. M. Jung, J. Mahmood, I. Y. Jeon, J. B. Baek, *Adv. Funct. Mater.* **2017**, *27*, 1.
[21] B. Li, S. W. Chien, X. Ge, J. Chai, X. Y. Goh, K. T. Nai, T. S. A. Hor, Z. Liu, Y. Zong, *Mater. Chem. Front.* **2017**, *1*, 677.
[22] Z. Q. Liu, H. Cheng, N. Li, T. Y. Ma, Y. Z. Su, *Adv. Mater.* **2016**, *28*, 3777.
[23] T. Meng, M. Cao, *Chem. Eur. J.* **2018**, *24*, 16716.
[24] S. L. Candelaria, Y. Shao, W. Zhou, X. Li, J. Xiao, J.-G. Zhang, Y. Wang, J. Liu, J. Li, G. Cao, *Nano Energy* **2012**, *1*, 195.
[25] Y. Ji, L. Huang, J. Hu, C. Streb, Y. Song, *Energy Environ. Sci.* **2015**, *8*, 776.
[26] J.-C. Liu, Q. Han, L.-J. Chen, J.-W. Zhao, C. Streb, Y.-F. Song, *Angew. Chem. Int. Ed.* **2018**, *57*, 8416; *Angew. Chem.* **2018**, *130*, 8552.
[27] M. Blasco-Ahicart, J. Soriano-Lopez, J. J. Carbo, J. M. Poblet, J. R. Galan-Mascaros, *Nat. Chem.* **2018**, *10*, 24.
[28] A. V. Sankarraj, S. Ramakrishnan, C. Shannon, *Langmuir* **2008**, *24*, 632.
[29] S. Zhang, O. Oms, L. Hao, R. Liu, M. Wang, Y. Zhang, H. Y. He, A. Dolbecq, J. Marrot, B. Keita, L. Zhi, P. Mialane, B. Li, G. Zhang, *ACS Appl. Mater. Interfaces* **2017**, *9*, 38486.
[30] R. Liu, G. Zhang, H. Cao, S. Zhang, Y. Xie, A. Haider, U. Kortz, B. Chen, N. S. Dalal, Y. Zhao, L. Zhi, C.-X. Wu, L.-K. Yan, Z. Su, B. Keita, *Energy Environ. Sci.* **2016**, *9*, 1012.
[31] Y. Umena, K. Kawakami, J.-R. R. Shen, N. Kamiya, *Nature* **2011**, *473*, 55.
[32] P. E. M. Siegbahn, *Acc. Chem. Res.* **2009**, *42*, 1871.
[33] Y. Ji, J. Hu, J. Biskupek, U. Kaiser, Y.-F. Song, C. Streb, *Chem. Eur. J.* **2017**, *23*, 16637.
[34] X. Yu, T. Hua, X. Liu, Z. Yan, P. Xu, P. Du, *ACS Appl. Mater. Interfaces* **2014**, *6*, 15395.
[35] X. Zhou, Z. Xia, Z. Zhang, Y. Ma, Y. Qu, *J. Mater. Chem. A* **2014**, *2*, 11799.
[36] Y. Cheng, P. K. Shen, S. P. Jiang, *Int. J. Hydrogen Energy* **2014**, *39*, 20662.
[37] J. Wu, Y. Xue, X. Yan, W. Yan, Q. Cheng, Y. Xie, *Nano Res.* **2012**, *5*, 521.
[38] B. Schwarz, J. Forster, M. K. Goetz, D. Yücel, C. Berger, T. Jacob, C. Streb, *Angew. Chem. Int. Ed.* **2016**, *55*, 6329; *Angew. Chem.* **2016**, *128*, 6437.
[39] B. Schwarz, J. Forster, M. H. Anjass, S. Daboss, C. Kranz, C. Streb, *Chem. Commun.* **2017**, *53*, 11576.
[40] J. Hu, Y. Ji, W. Chen, C. Streb, Y.-F. Song, *Energy Environ. Sci.* **2016**, *9*, 1095.
[41] W. Ling-Ling, H. Hao, R. A. Paredes Camacho, W. Ai-Min, C. Guo-Zhong, *J. Inorg. Mater.* **2017**, *32*, 135.
[42] J. G. Wang, H. Liu, H. Liu, Z. Fu, D. Nan, *Chem. Eng. J.* **2017**, *328*, 591.
[43] J. L. Junta, M. F. Hochella Jr., *Geochim. Cosmochim. Acta* **1994**, *58*, 4985.
[44] H. Xu, J. Wan, H. Zhang, L. Fang, L. Liu, Z. Huang, J. Li, X. Gu, Y. Wang, *Adv. Energy Mater.* **2018**, *8*, 1.
[45] U. A. Paulus, T. J. Schmidt, H. A. Gasteiger, R. J. Behm, *J. Electroanal. Chem.* **2001**, *495*, 134.
[46] K. J. J. Mayrhofer, D. Strmcnik, B. B. Blizanac, V. Stamenkovic, M. Arenz, N. M. Markovic, *Electrochim. Acta* **2008**, *53*, 3181.
[47] W. Tian, C. Wang, R. Chen, Z. Cai, D. Zhou, Y. Hao, Y. Chang, N. Han, Y. Li, J. Liu, F. Wang, W. Liu, H. Duan, X. Sun, *RSC Adv.* **2018**, *8*, 26004.
[48] B. You, F. Kang, P. Yin, Q. Zhang, *Carbon* **2016**, *103*, 9.
[49] W. Song, Z. Chen, C. Yang, Z. Yang, J. Tai, Y. Nan, H. Lu, *J. Mater. Chem. A* **2015**, *3*, 1049.
[50] L. Hao, S. Zhang, R. Liu, J. Ning, G. Zhang, L. Zhi, *Adv. Mater.* **2015**, *27*, 3190.
[51] Y. C. Kimmel, X. Xu, W. Yu, X. Yang, J. G. Chen, *ACS Catal.* **2014**, *4*, 1558.
[52] Y. Gorlin, T. Jaramillo, *J. Am. Chem. Soc.* **2010**, *132*, 13612.
[53] L. Zhao, S. Lin, K. Bi, C. Liang, Y. Du, J. Liu, H. Yang, D. Fan, Y. Wang, M. Lei, *J. Solid State Electrochem.* **2017**, *21*, 1743.
[54] S. Wang, Y. Sha, Y. Zhu, X. Xu, Z. Shao, *J. Mater. Chem. A* **2015**, *3*, 16132.
[55] G. L. Tian, M. Q. Zhao, D. Yu, X. Y. Kong, J. Q. Huang, Q. Zhang, F. Wei, *Small* **2014**, *10*, 2251.
[56] A. P. Tiwari, D. Kim, Y. Kim, H. Lee, *Adv. Energy Mater.* **2017**, *7*, 1602217.

Manuscript received: March 26, 2019
Revised manuscript received: May 18, 2019
Accepted manuscript online: May 20, 2019
Version of record online: July 28, 2019